7-2-2012

Planar shock wave interaction with a multiphase cylinder

Joseph Conroy

Joseph Conroy

Candidate

Mechanical Engineering

Department

This thesis is approved, and it is acceptable in quality and form for publication:

Approved by the Thesis Committee:

Peter Vorobieff, Chairperson

Randall Truman

Richard Nygren

PLANAR SHOCK WAVE INTERACTION WITH A MULTIPHASE CYLINDER

A study of Richtmyer-Meshkov Instability and Particle Lag Instability

by

Joseph E. Conroy

B.S. in M.E., University of New Mexico, 2010

Submitted to the Graduate Faculty
of the School of Engineering
in partial fulfillment of
the requirements for the degree of
Master of Science
in
Mechanical Engineering

University of New Mexico

2012

Acknowledgments

I would like to thank all of those who have supported me, assisted me, and inspired me during my research at UNM. I would especially like to thank God for all of the opportunities I have been given in life. I have been blessed and and I am full of gratitude.

PLANAR SHOCK WAVE INTERACTION WITH A MULTIPHASE CYLINDER

A study of Richtmyer-Meshkov Instability and Particle Lag Instability

by

Joseph E. Conroy

B.S. in M.E., University of New Mexico, 2010

M.S. in M.E., University of New Mexico, 2012

Abstract

We present an experimental study that visualizes the effects of a planar shock front passing through air (or SF_6) randomly seeded with glycol droplets or smoke particles. It was observed, using a high-speed multiple-CCD (charge coupled device) camera, that an instability occurs as the shock wave bypasses the slow-moving column of gas. This produced evident perturbation at the interface. The flow morphology of the gas column consists of a pair of counter-rotating vortices that develops downstream from the initial conditions as well as some secondary instabilities (in certain cases). Some images also show a trailing tail due to larger particles lagging behind the flow. The data and images obtained in the experiments were gathered using a tilt-able shock tube made of solid stock aluminum, two green-light lasers, and other high-speed diagnostics. Our experimental data cover a range of Mach numbers from 1.22 to 2.02. Each experimental run was performed with the shock tube in the horizontal position, causing only 2-D visualization effects.

Contents

List of Figures

Chapter 1

Introduction

Richtmyer-Meshkov instability (RMI) [1,2] is a hydrodynamic instability that is triggered by impulsively accelerating two fluids of different densities. This causes a baroclinic vorticity deposition on the density interface. As a result, any initial perturbations on the interface grow with time and mixing of the fluids ensues. The perturbation growth is initially linear (possibly after perturbation phase inversion), then shows signs of non-linearity, and later becomes turbulent. RMI can be achieved by accelerating in the light-to-heavy (ex: Air-to-SF_6) gas direction or in the heavy-to-light gas direction.

RMI can be produced in two different ways. One way is by shock acceleration of compressible gases; the other is by impulsive acceleration of effectively incompressible fluids. In the compressible case, the mechanism responsible for the instability is due to a misalignment in the gradients of pressure p and density ρ depositing vorticity ω at the interface. For the case of incompressible fluids, the misalignment of the gradient of acceleration and the gradient of density are what causes the deposition of vortices on the interface.

In our experiments, we observe a new phenomenon that produces results similar to RMI. Instead of having a gas-gas or fluid-fluid density interface, we are impulsively accelerating a column of air seeded with glycol droplets. Since there is no density

interface present, the underlying mechanism is entirely different from RMI. The details of both instabilities are explained in the theory section below.

1.1 Theory

In RMI, the passage of a shock wave through the interface of two gases of different densities results in the mixing of the two fluids due to the perturbed interface. A small two-dimensional (2D) perturbation produces a pair of counter-rotating vortices whose roll-up is caused by the initial misalignment between the gradient of pressure (or in the case of incompressible RMI, the direction of acceleration) and the gradient of density [3]. The misalignment is almost directly proportional to the cross product of the two parameters [4]. The cross product of the gradient of density and the gradient of pressure ($\nabla\rho \, x \nabla P$) are part of the curl of the Navier-Stokes equation.

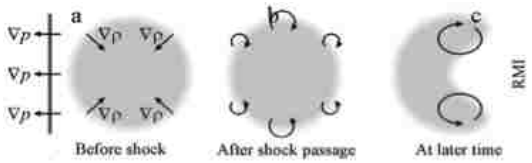

FIG. 1. Schematic of the underlying mechanism for RMI. The instability is created by a misalignment between the pressure gradient on the shock wave and the density gradient on the interface of the two fluids. In this case, the two fluids are compressible gases of different densities. - [4]

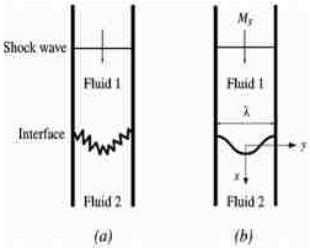

FIG. 2. a.)Discontinuous multi-mode interface. b.)Discontinuous single-mode interface. - [5]

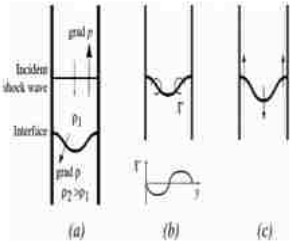

FIG. 3. a.)Misalignment in density and pressure gradients. b.)Vorticity deposition and intensity vortex sheet. c.)Subsequent deformation of the interface. - [5]

Chapter 1. Introduction

Richtmyer [1] developed the theory behind RMI using assumptions similar to those used in finding Rayleigh-Taylor instability (RTI), which was observed and explained by Lord Rayleigh [6] and later rigorously theoretically described by G.I. Taylor [7]. Richtmyer developed a linear model that measured the growth rate amplitude of a sinusoidal perturbation developed on a density interface. This amplitude is found using

$$\frac{da(t)}{dt} = \dot{a}_{1M} = kAa_0 u_c, \tag{1.1}$$

where k is the wave number of the perturbation (= $2\pi/\lambda$), A is the post-shock Atwood number (dimensionless density ratio) (= $(\rho_0 - \rho_1)/(\rho_0 + \rho_1)$) where the shock moves from fluid 1 to fluid 0, u_c the change in interface velocity due to the action of the shock and a_0 is an appropriate initial amplitude [5].

This derivation models the effect of the shock on the interface of a flow assumed to be incompressible. The amplitude equation used above is a simple approximation in a linearized form of the compressible Euler equations, which has resulted in one partial differential equation. The solution of this PDE has been investigated numerically and semi-analytically and both have proven to have results in good agreement [5].

Non-linear (N-L) models have also been developed to measure the amplitude of the perturbation at the interface once it grows past a certain size. This is due to the fact that the compressible linear theory and the impulsive model no longer apply for this case [5]. This N-L growth leads to secondary instabilities and nonlinearities that eventually leads to turbulence. RMI-induced turbulence is a topic that has shown much interest from

experimentalists and numericists [3]. Coupling numerics with experiment can greatly improve the understanding of transition to turbulence. One can use the numerics as a starting point and later validate these codes with experiments. This makes it possible to make plausible conclusions about the growth of the width of the turbulent mixing zone and other scales in the flow [3].

It was also shown by Richtmyer that using linear RTI theory to model the irrotational flow of two incompressible fluids of different densities and velocity potentials yields the amplitude equation for this specific case. This is given by

$$\ddot{a} = -kAGa\,, \tag{1.2}$$

where G is represented as the product of a velocity jump and a Dirac delta function, $G = \Delta V \delta(t)$, where ΔV is the change in velocity due to the shock wave passage [4]. The vorticity deposited by the shock can be measured analytically [3] by using the curl operator on the Navier-Stokes equation and disregarding the diffusive terms

$$\frac{D\omega}{Dt} = \frac{1}{\rho}\nabla\rho x \nabla P. \tag{1.3}$$

The diffusive terms are not significant until much further downstream where the vortices begin to dissipate and are therefore omitted. After the passage of the shock wave, the column of gas compresses and this affects the density and pressure of the gas column. The governing equation for the change in density as a consequence of gas compression [8] is given by

$$\frac{\rho_2}{\rho_1}=\frac{(\gamma+1)M_1^2}{(\gamma-1)M_1^2+2}, \tag{1.4}$$

where the subscripts 1 and 2 define the states before and after the passage of the shock wave, respectively.

Also, γ is the ratio of specific heats (c_p/c_v) and is considered nearly constant in this case since the change in temperature is insignificant. The Mach number $M_1=v_1/c$, where v_1 is the velocity of the shock front and c is the speed of sound. Similarly, the pressure ratio is governed by

$$\frac{\rho_2}{\rho_1}=\frac{2\gamma}{\gamma+1}M_1^2-\frac{\gamma-1}{\gamma+1} \tag{1.5}$$

In the case of our experiments, there is no gas-gas density interface present. We are impulsively accelerating air seeded with macroscopic glycol droplets or sub-micron sized smoke particles, which produces morphology similar to RMI. Since the density interface is absent, the underlying mechanism is much different than that of RMI. Although the embedded phase may have a relative velocity of zero prior to the shock acceleration, it has a higher density than the surrounding flow, which causes the droplets to "lag behind" the gas after the shock acceleration [4]. Due to the compressibility effects, the transient forces are much greater than the quasi-steady drag [9], which leads to a greater momentum exchange between the droplets or particles and the surrounding flow. This causes an entrainment of particles or droplets in the flow that is driven by viscosity and

has a lower local velocity than the unseeded gas. Shear between the areas of lower and higher velocities eventually leads to the development of a pair of counter-rotating vortices. We call this particle lag instability (PLI) and it can be seen in a number of applications.

In both RMI and PLI, there is a compression phase and a change in density following the passage of the shock wave. Although these two instabilities share similar morphologies, PLI develops much slower than RMI. The different mechanisms are compared in Fig. 4, which also displays Fig. 1 in the top row. A physical explanation for that will be provided in the following section.

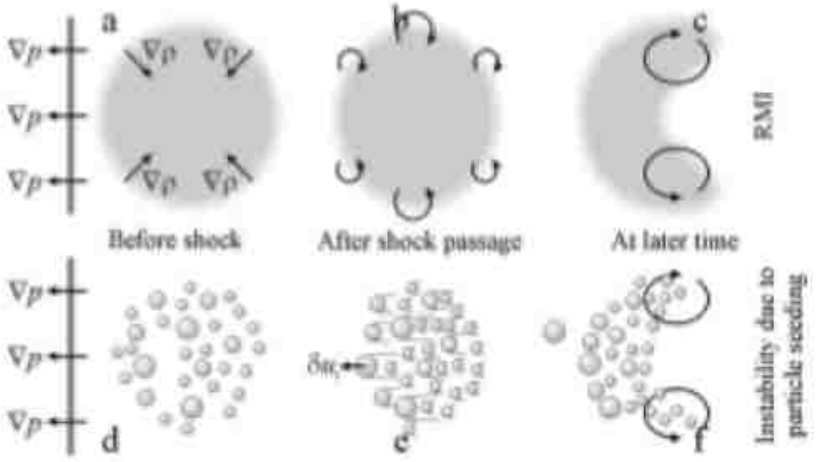

FIG. 4. Schematic comparison of RMI (a-c, top row) and PLI (d-f, bottom row). RMI is driven by misalignment between the pressure gradient on the shock (p, a, d) and density gradient on the interface between two gases. This misalignment leads to vorticity deposition on the interface (b), and to subsequent vortex roll-up (c). In the seeded flow (d), there is no macroscopic density interface. Immediately after shock interaction, seeding particles lag behind the gas accelerated to piston velocity, acquiring relative velocities. (e) and interacting with the surrounding gas. As the particle and gas velocities reach equilibrium, the average velocity of the medium is lower than that of the unseeded gas, leading to shear and vortex roll-up (f). – [4]

Chapter 1. Introduction

The drag force on a small impulsively accelerated spherical droplet and the time required for it to match the velocity of the surrounding flow can be estimated analytically using Stokes approximation [10]. Stokes equations are given by the following two equations:

$$\nabla u = 0 \tag{1.5}$$

$$\frac{\partial u}{\partial t} = \frac{-1}{\rho}\nabla p + v\nabla^2 u. \tag{1.6}$$

For uniform flow past a sphere, the Stokes equations yield a drag force equal to $F = 6\pi\mu Uae_x$, where U is the flow velocity, a is the radius of the droplet, μ is the dynamic viscosity, and e_x is the x-directional unit vector [10]. The larger droplets have a greater radius, causing the drag force to rise, according to Stokes as well as a rise in Reynolds number $Re = U\,d/v$, where U is the post-shock relative particle velocity and v the kinematic viscosity of the embedding gas. Although this is an approximation of the drag force, a real shock-droplet interaction is much more complex due to the aforementioned compressibility effects [9].

There are several parameters that affect RMI. The Mach number of the shock wave M and the Atwood number A of the two fluids being accelerated are most important. In the case of PLI, instead of the "traditional" Atwood number (dimensionless density difference), an effective Atwood number has to be introduced, based on average densities. Other factors contributing to RMI (or PLI) evolution in a shock tube experiment include the effects of the walls of the shock tube interacting with the flow morphology; primarily

near the injection site of the initial conditions, the injected particle size, and the initial conditions geometry. In the sections following the theoretical chapter and the description of the experimental setup, the contributions of these parameters and factors will be discussed, leading to some conclusions and suggestions for future work.

1.2 Applications

There are many applications where PLI can be seen and is of great importance. In the case of biological warfare, the question involving PLI would be the effect of shock (e.g., from an explosion) on chemical or biological agents suspended in air, with PLI contributing to their transport and thus affecting the contamination zone.

PLI may also play a role in supersonic combustion applications involving shock interaction with jets of fuel droplets [4]. An example would be a scramjet where combustion requires the fuel to be injected, mixed, and burned in milliseconds. Understanding the physics behind the mixing of supersonic compressed air and droplets of fuel may bring us closer to achieving the theoretical Mach numbers of a Scramjet, which are in the hypersonic range and up to $M = 25$ [11].

1.3 History of Shock-Driven Flow Studies

There are various experimental setups used to study RMI. The shock tube remains one of the primary ways of showing compressible RMI. In 1969, E.E. Meshkov [2] used a horizontal shock tube to prove Richtmyer's theory and show the instability. The shock

tube consisted of a pressurized driver section and a driven section, kept at atmospheric pressure, that were separated by 4 layers of cellulose acetate film, each at 0.2 mm thick. The instability was captured using an SFR-3M camera and an IFK-120 light source. This produced shadowgraph images of RMI at the interface of the two gases, which pioneered this dynamic field of shock-driven fluid mechanics.

Since the discovery of RMI in experiment, there have been various other methods used that have improved visualization and ease of experiment. Figure 5 shows an example that Jacobs and Sheeley [12] reported in 1995 that produces RMI by providing an impulse to two miscible liquids (without using a shock wave); salt water on the bottom half and the fresh water on the top half.

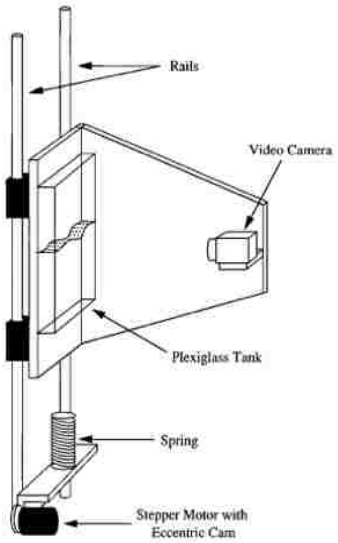

FIG. 5. Drop tank experimental setup. – [12]

Chapter 1. Introduction

The impulse is generated by releasing the tank containing the two fluids (purely gravity driven) and allowing it to strike a spring that has been placed in a vertical position below the apparatus. This causes a rapid deceleration of the tank, which in turn results in the production of an impulse propagating through the medium. The solution is also lightly shaken with a sinusoidal motion in the lateral direction prior to releasing the tank, which produces standing waves. The initial perturbations are created using a stepper motor. Changing the input signal to the stepper motor can control the wavelength of the interface pattern. Figure 6 illustrates some of the results that were obtained by Jacobs and Sheeley using a VHS tape recorder, CCD camera, and ambient light. A dye was also added to differentiate the two fluids from each other.

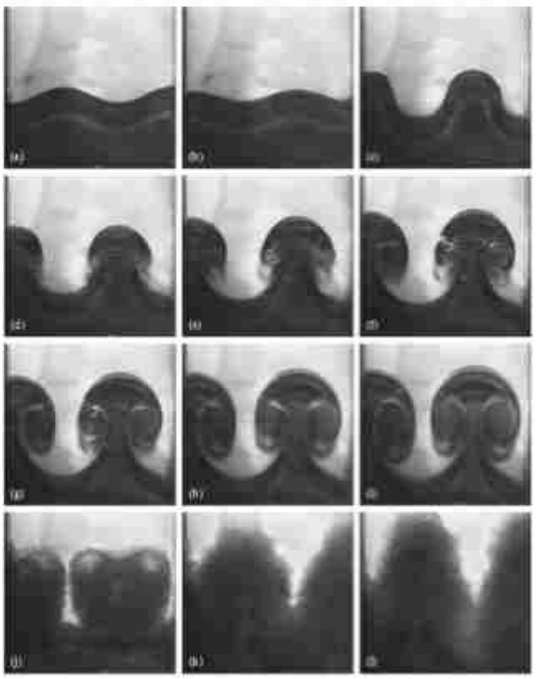

FIG. 6. Initial interface shape right before contact with the springs in 4(a) and the sequence occurs about every 65 ms/frame. – [12]

Chapter 1. Introduction

There is a re-acceleration that happens due to a second bounce between frames (i) and (j) [12]. By taking the second derivative of the tank position function X vs. time, the acceleration $\ddot{X}$ was obtained. By adding gravity to the measured acceleration, the following plot of "virtual gravity" that the fluids experience vs. time was found.

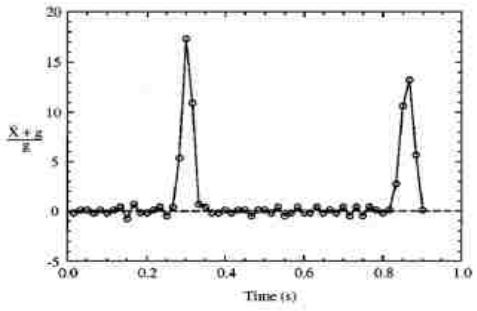

FIG. 7. "Virtual gravity" experience by the fluids versus time. – [12]

A few different models were used to scale the initial growth rates of the instability and plot them against dimensionless time scales. Most of the growth curves collapsed to a single curve quite nicely.

The experiment showed above created an impulsive acceleration in two incompressible fluids with different densities by using a drop tank setup. It is also common to model compressible RMI using a shock tube and high-speed equipment. This is an effective way to model RMI, but it is difficult to achieve due to the timescales being very small; on the order of microseconds. There are many different shock tube and diagnostic systems that have been used to visualize RMI.

Chapter 1. Introduction

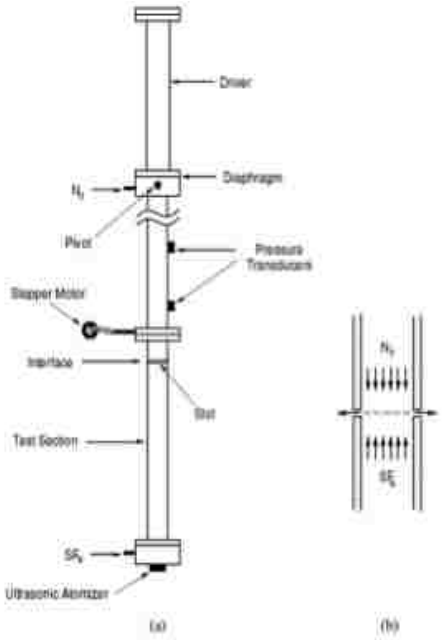

FIG. 8. Vertical shock tube apparatus. – [13]

Figure 8 shows a vertical shock tube [13] that uses a driver section, separated from the driven by a diaphragm made of Mylar. In the bottom section, SF_6 is fed through, whereas in the middle section N^2 is injected. There is now a light-to-heavy gas-gas density interface that is “flat” (parallel to the floor). Similar to the previous setup, an adjustable stepper motor is used to initially perturb the interface and produce standing waves. The initial velocity of these waves is much smaller than that of the instability, so the effect on the initial instability growth rate is very modest [12].

A fog machine was placed at the bottom of the shock tube to provide liquid droplets to the SF_6 that act as tracer particles. Once the initial conditions were established, the driver section was pressurized with helium and then released by puncturing the

diaphragm. This produced a weak shock wave (M = 1.1) that traveled down the shock tube and struck the initially perturbed interface producing RMI. The dimensionless Atwood number is A = ~0.67 and showed to be more significant in the case of a gas-gas density interface, as opposed to the aforementioned liquid-liquid interface [12, 13]. The resulting instability yielded much more top-to-bottom asymmetry than the previous experiment. The discrepancy between experimentally measured and predicted growth rates has been attributed to strength and porosity effects of the membrane used to separate the gases in shock tube experiments and is also due to boundary layer effects [5].

Kumar and others of Los Alamos National Labs and Vorobieff of the University of New Mexico experimented using a planar shock tube and impulsively accelerated a light-to-heavy cylindrical interface. In this setup, a Mach 1.2 planar shock wave impulsively accelerates one of five different configurations of heavy gas (SF_6) cylinders surrounded by lighter gas (air), producing one or more pairs of interacting vortex columns [14].

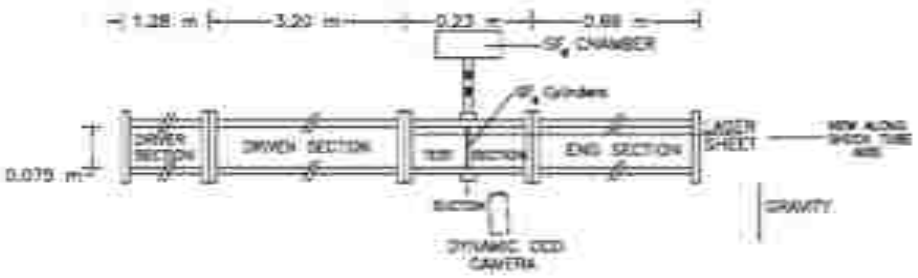

FIG. 9. Horizontal shock tube apparatus. – [14]

The shock tube consists of four separate sections; driver, driven, test, and run-off sections. A polypropylene diaphragm separates the driver and driven sections and is punctured using a solenoid with razor blades on one end. This releases the shock wave

allowing it to pass through the driver section and strike the curtain of SF_6 that is passed through the test section and stabilized with a light suction on the bottom. This is all captured using planar laser-induced fluorescence (PLIF) and a back-illuminated Apogee CCD (charge-coupled device) camera for dynamic visualization.

Here, feeding SF_6 through a container holding acetone creates a curtain of gas cylinders. The acetone is used for visualization with PLIF (planar laser-induced fluorescence) technique that uses fluorescence in acetone when the latter is illuminated with an ultraviolet (UV) laser sheet. The curtain is impulsively accelerated by a planar shock wave, producing a pair of counter-rotating vortices on the interface of each cylinder.

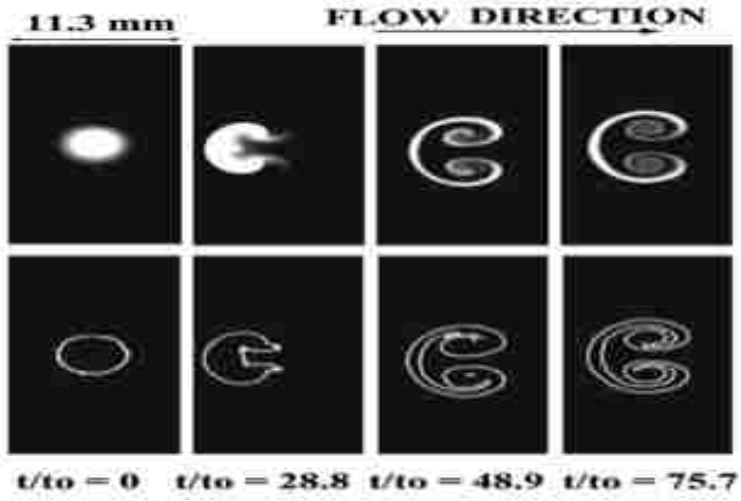

FIG. 10. Top row) A sequence of multiphase SF_6 RMI. A single cylinder is used in this case (1C). Bottom row) Contour lines simulating the morphology. – [14]

In this experiment, there were about 700 images taken anywhere between t = 0 μs to t = 500 μs at 15 μs intervals. In Fig. 10 above, it can be seen in the first frame that the initial conditions are perfectly round. Once the shock wave has passed, the flow

morphology shows a symmetric pair of counter-rotating vortices that develops the further downstream the flow travels. The bottom row of Fig. 10 shows contour lines that model the experiment, which are comparable.

The case shown above (Fig. 10) is modeling only one gas cylinder. An image of a double cylinder (2C) gas curtain is shown below in Fig. 11.

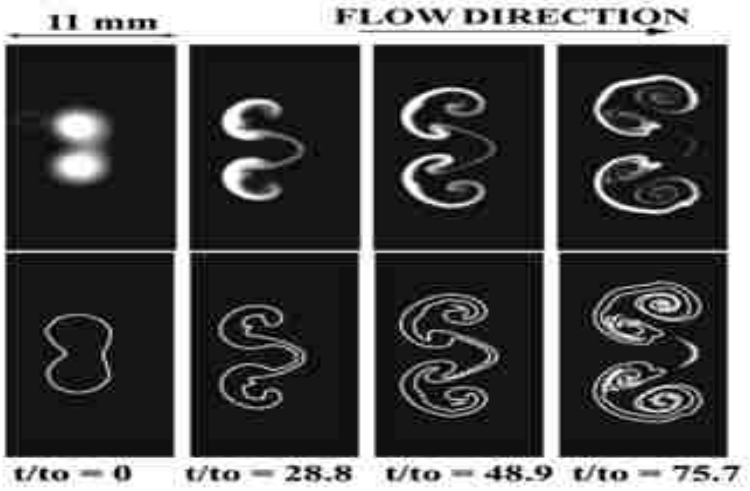

FIG. 11. Top row) A sequence of multiphase SF_6 RMI. A two cylinder curtain is used in this case (2C). Bottom row) Contour lines simulating the morphology. – [14]

Since there is more than one gas cylinder being modeled here, there is going to be some interaction between each cylinder. This shock interaction between the two gaseous cylinders creates two vortex pairs. Due to there being density gradients of smaller magnitude because of diffusion between the cylinders, the inner two vortices are weaker than the outer vortices. This is proven by the fact that there is more roll up in the outer two vortices than in the inner two vortices [14].

Figure 12 shows PLIF visualization of the early stages of a shock-accelerated single

cylinder at Mach 1.2. The shock is from left to right and starts at $t = 0$ μs and ends at $t = 30$ μs.

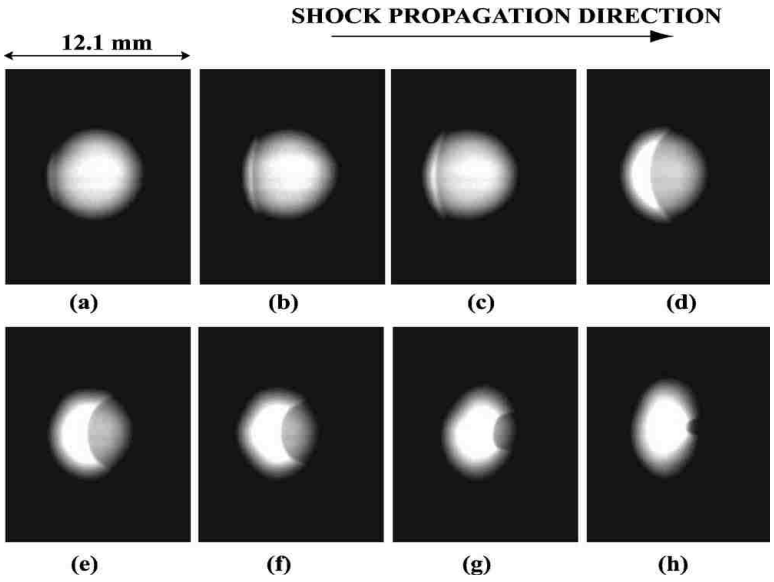

FIG. 12 Mach 1.2 shock-accelerated gas cylinder resulting from an 8 mm diameter nozzle. Frames (a) through (h) show the time sequence at regular time intervals: (a) t = 0 μs and (h) t = 30 μs. – [14]

In Fig. 14(h), it can be seen that there is lensing effect that occurs on the downstream side of the cylinder during the compression phase. The cusp that develops can be accredited to the large pressures produced by this focusing.

The next chapter will cover our experimental setup and some of the design changes made to improve the functionality of our system.

Chapter 2

Experimental Setup and Diagnostics

2.1 Overview

There are three key subsystems in our experimental setup: a tilt-able shock tube with an adjustable wall mount, the injection system, and visualization/imaging diagnostics. Each of these subsystems is unique in its design and functionality and is a vital part in capturing PLI and RMI.

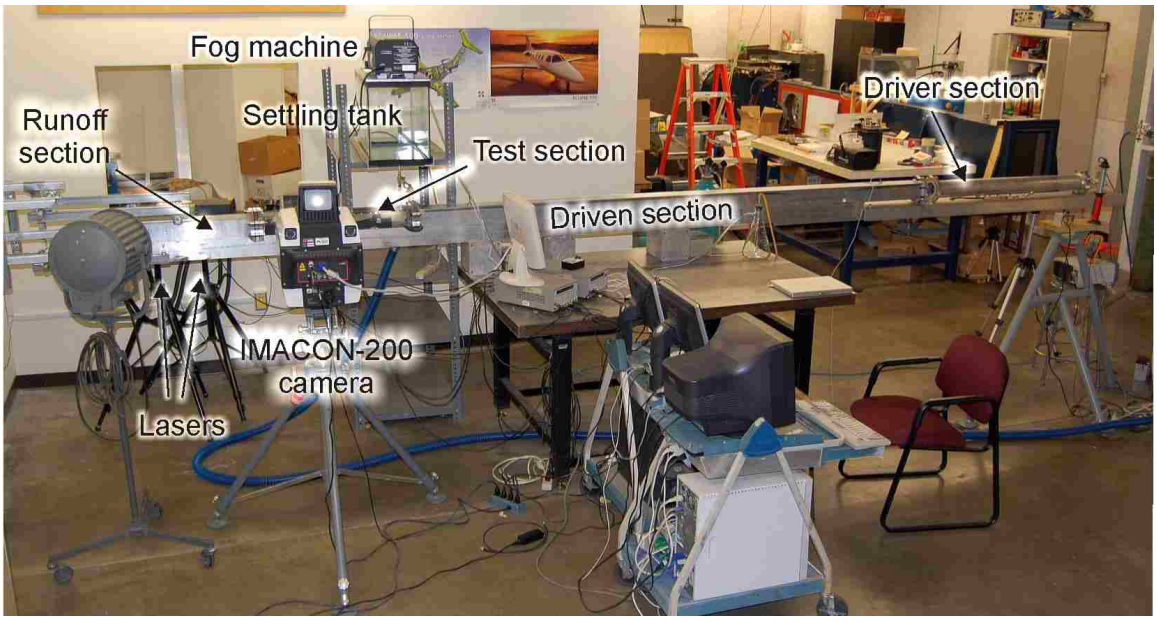

FIG. 13. Photograph of UNM's shock tube facility.

The shock tube is made of 6061T6 solid-stock aluminum with a 75 x 75 mm cross-section and is divided into four sections: driver, driven, test, and runoff. The driver

system includes a steel rod that glides along linear bearings and is driven by an electronic solenoid on one end. On the other end of the rod are four utility blades that form a sharp point. A thin sheet of Mylar (or multiple sheets for higher pressure) separates the driver

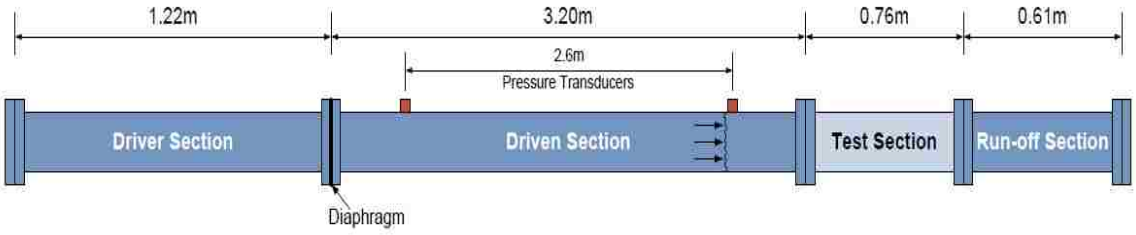

FIG. 14. Diagram of the shock tube and its individual sections.

and driven section allowing the driver section to be pressurized with helium to a desired pressure. The solenoid then forces the blades through the diaphragm and releases the shock wave.

The driven section has two pressure transducers that are spaced 2.59 m apart. Each transducer sends a signal to the diagnostics system. Pressure signal acquisition in the latter is triggered by a rise in pressure from the passing of the shock past the first (upstream) transducer. The second (downstream) transducer is used to trigger components of the optical diagnostics subsystem. After the shock wave travels past the driven section, it then enters the test section where it strikes the initial conditions. The shock wave passes through the test section and either dissipates out of the open end of the run-off section or reflects off a wall (or window) terminating the run-off section.

The adjustable wall mount allows for two directions of motion. One is in the vertical direction and the other is in the angular direction, which allows the shock tube to

be tilted to produce oblique shock waves. It is made up of steel Unistrut, round solid-

FIG. 15. Wall mount system setup for planar shock waves.

stock and concrete reinforcement bolts. Two large pieces of Unistrut act as vertical rails to facilitate in raising and lowering the shock tube and are connected to the wall with reinforced concrete bolts. Between the wall and the rails are pieces of polyurethane rubber. These pieces of rubber act as shock absorbers for when the shock tube is fired. Connected to the rails are shorter pieces of Unistrut that allow the shock tube to protrude out of the wall. The two round solid-stock pieces are fitted in round brackets attached to the Unistrut rails and allow for tilting of the shock tube.

The anti-recoil system is needed to prevent the shock tube from moving during experiments. Preventing movement in the shock tube is necessary for proper data acquisition. Prior to each shot, a background image is taken before the initial conditions begin to flow. This background is then subtracted from the image captured during experiment. If the shock tube were to move during the experiment, the optical view would change resulting in a misalignment in the background image and the experimental image.

2.2 The Injection System

The injection system starts with a settling tank (12"W x 20"L x 16"D) filled with either air or SF_6 seeded with glycol droplets or sub-micron sized smoke particles. The lid on the tank is made of 0.5" thick aluminum that is used to dissipate heat produced by the fog machine that is located on top of the lid. The fog machine seeds the SF_6 or air with the glycol droplets through a port in the lid. There is a vertical nozzle that is 6.35 mm in diameter located on the bottom of the settling tank. The injection material is either driven by gravity (SF_6) (since its average density is higher than that of air) or fan-driven (air) through an apparatus that introduces a concentric co-flow of unseeded air to stabilize the slow-moving jet. In the case when the injected material is air with glycol droplets, the gravity-driven flow is assisted with a gentle overpressure at the top of the settling tank provided by an electric fan blowing through a square port (63 mm x 63 mm). This minimizes any three-dimensional initial perturbations on the interface of the column [4].

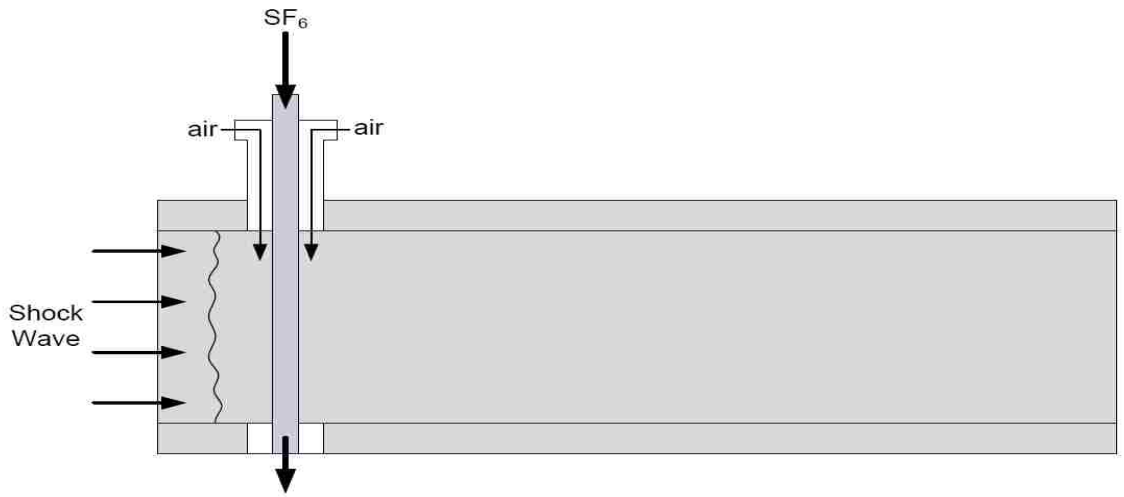

FIG. 16. Diagram of the injection system and concentric co-flow.

2.3 Diagnostics

A combination of an Apogee single-CCD camera (Fig. 17) and an Imacon 200 multiple-CCD camera (Fig. 18) were used to capture the instability. The Imacon uses multiple CCD modules to provide simultaneous framing and streak recording through a single optical axis, whereas the apogee uses a single CCD but with a better resolution. Each camera was fitted with a Sigma EX DG macro lens which has a 105 mm focal length and an f/2.8 f -stop.

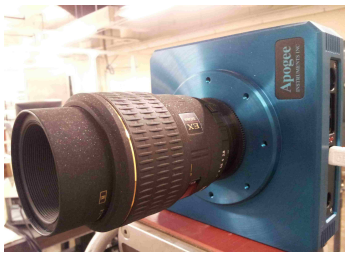

FIG. 17. Apogee single CCD camera.

FIG. 18. DRS Imacon 200 multiple CCD camera.

Chapter 2. Experimental Setup and Diagnostics

The cameras were controlled by a dedicated computer running Imacon 200 software of Maxim DL (for the Apogee CCD), which allowed us to capture the instability. Illumination was provided by two double-pulsed Nd-Yag green-light (532nm) lasers. This allowed us to capture up to four frames per experiment when using the Imacon.

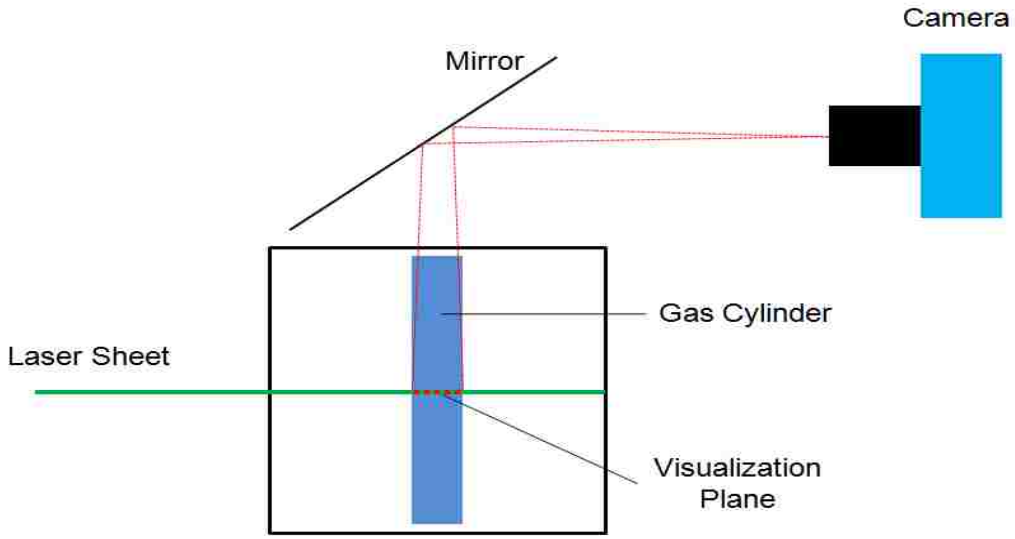

FIG. 19. Diagram of the camera and laser diagnostics.

After the shock passes the first pressure transducer, there is a pulse sent to a National Instruments NI-Scope program that is used for recording pressure traces. The shock then passes the second transducer where the second pulse is recorded. Knowing the time between each of the pulses and the distance between the transducers allows us to extract the theoretical Mach number from each experiment. The second transducer also triggers a delay generator, which compensates for the time it takes the shock wave to travel from the transducer to the location of interest where the camera is aimed. The delay

generator then triggers the camera and the lasers. The timing of the pulses and the camera exposures is adjusted with microsecond accuracy, based on the extent of the field of view and the Mach number of the experiment. This is to ensure that all the exposures are in the field of view of the camera.

2.4 Additional Design Changes

To increase the productivity and ease of experiments, the connection between the driver and driven sections was redesigned. The previous design used six to eight grade-A nuts and bolts to connect the two flanges together. During removal, the bolts would often strip and cause the nuts to become immovable. This made it nearly impossible to remove them without breaking the bolt or cutting off the nut with a grinding tool. Instead of using the nut and bolt system, a clamping system was designed that connected to the existing flanges to create a tight seal. The system includes two 2000-lb pull action toggle clamps with a U-bolt design.

FIG. 20. Pull action toggle clamp.

The U-bolt is made of steel and is 0.31 inches in diameter. This clamp was chosen based on the amount of force the driver section would apply to the interface of the two sections when pressurized. Knowing the diameter of the opening of the driver section and the given pressure associated, it was trivial calculating the applied force, since $P = F / A$. The force was calculated to be about 1150 lbs at M = 2.1. This Mach number was chosen since it is our highest operating Mach number. Applying a Factor of Safety (FoS) of 2.0 required clamps that could withstand a combined force of 2300 lbs. The 2000-lb clamps were chosen, which allowed for up to a theoretical 4000 lbs of force (or P = 500 psi).

To connect the clamps to the shock tube, two supports were created from solid-stock aluminum using a CNC (Computer Numerical Controlled) machine. The supports consist of three pieces each and are held together using grade-A flat head screws and bolts.

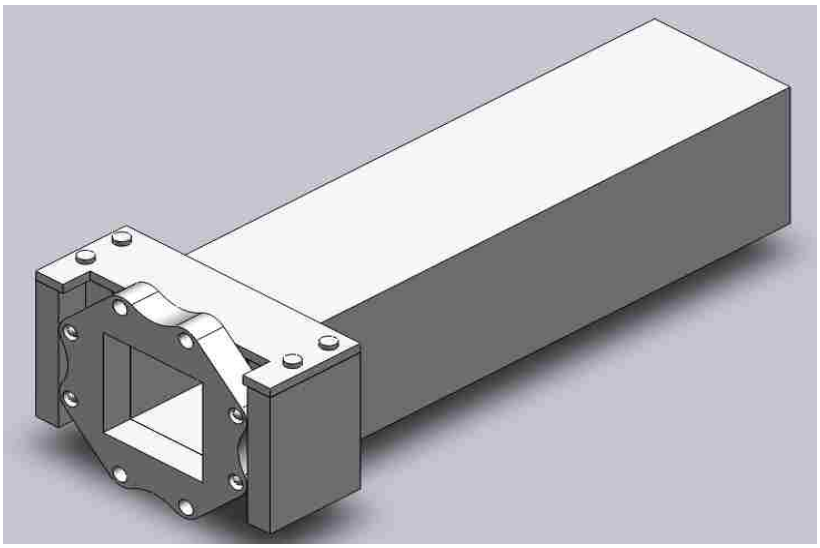

FIG. 21. Clamp support partial assembly.

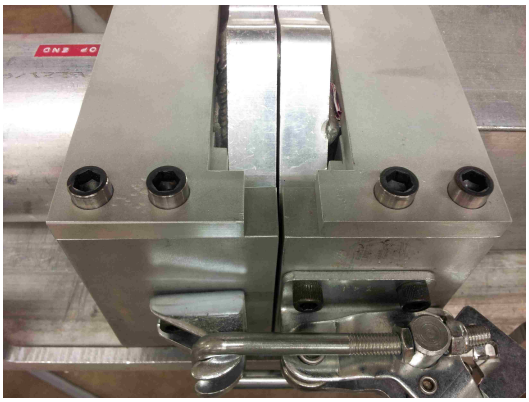

FIG. 22. Side view of clamp assembly.

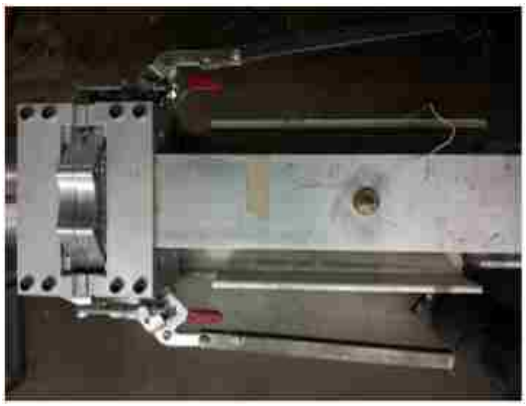

FIG. 23. Top view of clamp assembly.

The support sides were designed to lay flat against the sidewalls of each section to minimize stress on the flanges. A top piece was also added to minimize movement and make the supports more rigid. The clamp handles were customized and lengthened to allow the system to be easily locked.

Chapter 3

Results of Experiments

The following results were taken in the horizontal position using the aforementioned shock tube and diagnostics setup. I will present the results from experiments conducted at average Mach numbers of 1.22, 1.67, and 2.02. A comparison of Mach number as well as a comparison of RMI and PLI will be observed. The effects of other parameters such as the test section walls, particle size distribution, and the geometry of the IC's are assessed as well.

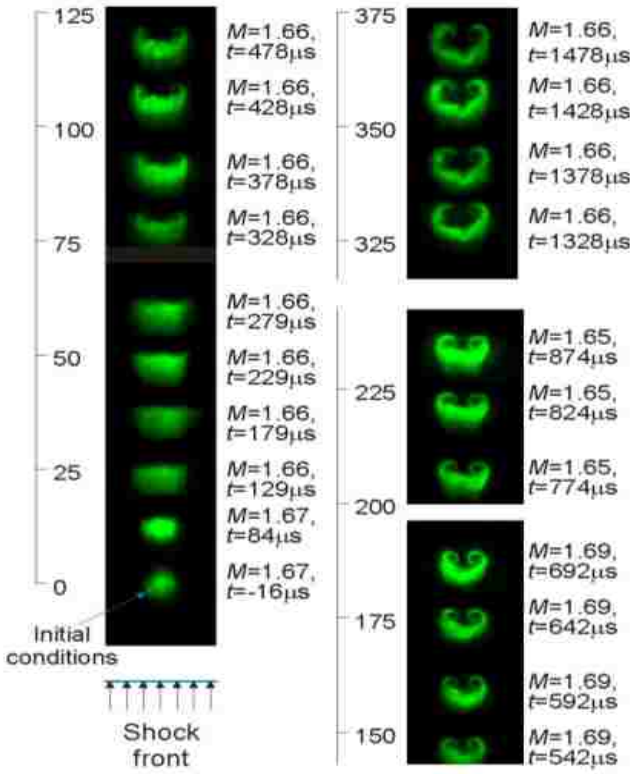

FIG. 24. A mosaic of six experimental images taken of a shock accelerated column of air and fog, yielding particle lag instability. The shock direction is from bottom to top. The Mach number was averaged to be M = 1.66 ± 0.02 and t = 0 is the time when the shock wave reaches the center of the initial conditions. Numbers listed on the left of the images correspond to downstream distance in mm – [4].

Chapter 3. Results of Experiments

Figure 24 shows a cross-sectional view of the evolution of PLI from $t = 0$ to $t =$ 1478 μs at an average Mach number M=1.66 ± 0.02. This gives us an insight to the early times morphology of the instability, which shows the compression phase followed by the development of counter-rotating vortices. The shock passage accelerates the surrounding medium to a piston velocity of about 303 m/s [4]. The droplets are about 850 times denser than air before shock compression, but only make up about 5% volume fraction of the injected material. In the earlier images of the sequence, you can see that the seeded area of the flow is starting to compress together with the embedding air. The larger particles (size estimated at 4 μm) are lagging in the flow and are further upstream, whereas the smaller particles (< 1 μm) form a line parallel with the shock front. The smaller particles exchange momentum with the air faster than the larger particles, which causes the latter to lag behind the shock-accelerated air for a longer duration. The shear between the areas of lower and higher velocities causes the pair of counter-rotating vortices to develop on the sides of the column. This can be seen from t = 328 μs to subsequent times further downstream.

3.1 RMI and PLI Comparison

Seeding the flow with solid particles (i.e. smoke) yields similar macroscopic morphologies to droplet seeded flow. This is an important observation since each individual glycol droplet interacts differently with the flow. For example, the droplets might deform, merge with one another, or break up in the flow. In Fig. 25, we compare

Chapter 3. Results of Experiments

PLI using smoke particles to PLI using glycol droplets as well as a comparison to RMI.

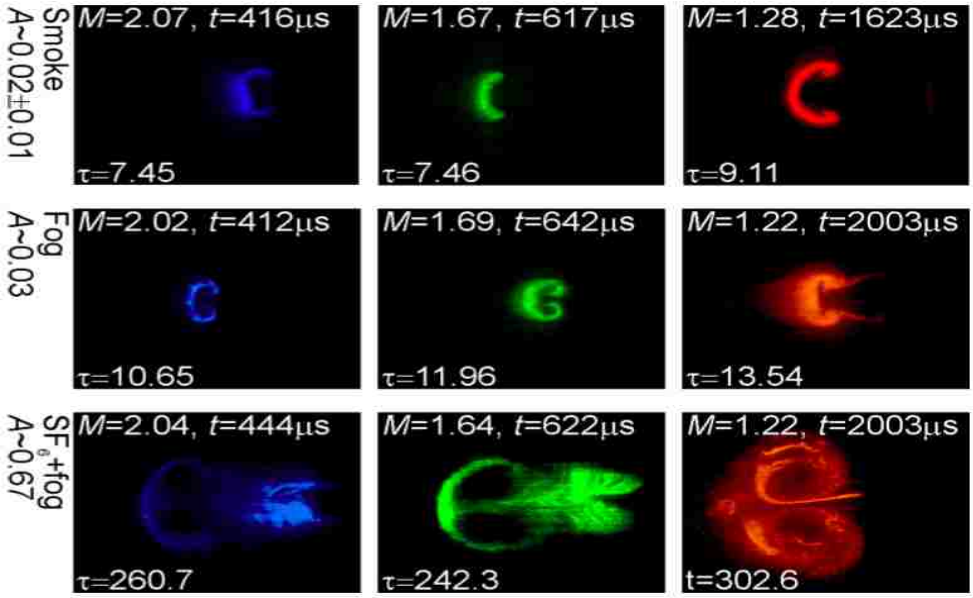

FIG. 24. Mach number study of injected medium consisting of air-smoke particles (top row), air-glycol droplets (middle row), and SF_6-glycol droplets (bottom row). The color-coding corresponds to the varying Mach number, where red is the lowest (M = 1.22), green is mid-range (M = 1.67), and blue represents the highest (M = 2.02). Each image was captured using a frame width of 152 mm to 181 mm. The flow is from left to right. Dimensionless τ is included as well as the time corresponding to downstream distance – [4].

The shock is traveling from left to right and it is apparent that there is a relatively weak correlation between the Mach number and the size of the instability. In the case of RMI, there are secondary instabilities that arise due to shear, also known as Kelvin-Helmholtz instability, and because of the pressure-density misalignment in the cores of the vortices causing a baroclinic instability. Due to the different speeds of shock propagation through the air and through the SF_6, a lensing effect emerges in the case of RMI, which produces the "spike" feature that can be seen downstream of the vortex pair in the bottom row of Fig. 25. There may be evidence of these small-scale structures in

the droplet-seeded flow much further downstream ($t > 1$ ms), but there was no evidence of a transition to turbulence. This is a similar feature shown by Kumar (Fig. 12) and is only evident in RMI experiments. As you can see, the instability has developed much quicker in the case of RMI than PLI. This means that the transition to turbulence will be much further downstream for the case of PLI.

For air-SF_6, the average density was measured (1.26 ± 0.01 kg/m3) and used to calculate the effective Atwood number, $\sim A = 0.03$. For air-smoke, $\sim A = 0.02 \pm 0.01$, since the consistency of smoke fluctuates between experiments. This measurement was accomplished by placing a container in the settling tank and allowing it to fill with either fog or smoke and then quickly trapping the matter with a lid. The container was then weighed with and without the particles/droplets using a high accuracy scale. This was repeated multiple times and averaged. Knowing the volume of the container and the weight of the particles, an average density was calculated. Since the effective Atwood number for PLI is much less than the Atwood number for RMI ($0.03 << 0.67$), Richtmyer's growth rate theory, given by Equation 1.1, shows that the interfacial growth of RMI is greater than PLI.

3.2 Growth of Perturbation

The top plot of Fig. 26 shows a comparison of the instability growth for RMI and the instability of the droplet-seeded air column as the function of downstream distance from the initial conditions. The data were acquired in about 200 experimental

runs (resulting in 572 amplitude measurements), conducted in the range of Mach numbers from 1.22 to 2.02. At the beginning of the experiment there is a quick rise in amplitude growth followed by a sudden decrease. This decrease occurs after shock compression and is also accredited to phase inversion effects on the downstream side of the gas cylinder for the case of RMI. As mentioned before, the growth amplitude grows much quicker and larger for the case of RMI and the Mach number dependence is rather weak [4].

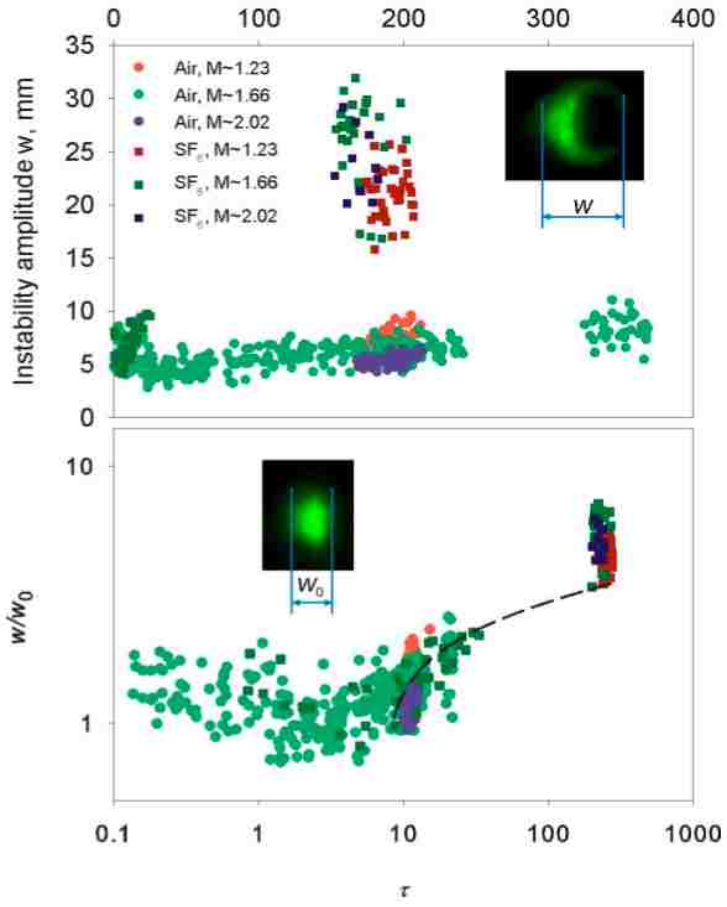

FIG. 26. Streamwise perturbation growth w as a function of downstream distance measured in dimensional (top) and dimensionless (bottom) coordinates. Bottom plot is a collapse of the data in the top plot using dimensionless coordinates proposed for studies of RMI [9].– [4]

Chapter 3. Results of Experiments

It has been reported [15] for cases of RMI that the perturbation growth curves of different Mach numbers can be collapsed by plotting them using a dimensionless temporal coordinate τ and by non-dimensionalizing the width by w_0. Dimensionless τ relates to the time after shock acceleration t as $\tau = 2kA|\Delta U|t$. The perturbation amplitude growth w is non-dimensionalized by w_0, which is the average minimum width of the perturbed column after the shock acceleration for each of the Mach numbers studied (M = 1.22, M = 1.67, and M = 2.02). This same principal can be applied to PLI.

In the bottom plot of Fig. 26, the growth curves have been non-dimensionalized and have collapsed fairly well according to Richtmyer's theory. The dashed curve is produced by using several flow parameters measured during the experiments for the SF_6-droplet column at $M \sim 1.67$ [16]. These are characterized by the wavenumber k given by the initial conditions, the post-shock minimal streamwise width of the perturbed column w_0, and the corresponding time t_0. These parameters are inserted into a semi-analytical formula developed from an earlier formula [17] that is known to describe nonlinear vortex growth after shock acceleration, although with a somewhat different initial geometry [16, 18]:

$$w(t) = 2\mathrm{k}^{-1}\sinh^{-1}[k^2\Gamma(t-t_0)+\sinh(kw_0/2)] \tag{3.1}$$

Here we can replace t with $x/|\Delta U|$. With this formula, we can curve-fit our experimental data for RMI at $M \sim 1.66$ using the shock-deposited circulation, which is not measured directly, as the sole fit parameter. After the curve is rescaled consistently

with the experimental data, it agrees reasonably well with both the measurements for RMI and the measurements for PLI [4].

Numerical calculations performed by Anderson [19] also hint at something possibly pertinent to both particle lag instability and "traditional" RMI. Recent numerical work suggests that a better collapse might be obtained with alternative amplitude scaling involving the square root of the Mach number. More experimental work will be needed to confirm this scaling.

3.3 Multiple Planes

A parametric study was conducted that involved multiple planes to provide data ensembles suitable for reconstruction of the 3-dimensional image of the flow morphology. These ensembles are shown in Fig. 27 (RMI) and in Fig. 28 (PLI). The instability evolution is from left to right and shows a time sequence that starts at 19 cm and increases by ~5 cm per image (50 μs spacing). One prominent factor of interest that has been assessed is the capability to visualize the flow near the walls of the shock tube. The walls have an effect on the flow morphology, particularly near the injection site. In Fig. 28, Mie scattering off droplets reveals vortex structure that develops due to particle lag instability. Note the absense of the spike due to shock focusing (found only in traditional RMI), explained by the fact that there is no macroscopic pressure gradient in the initial conditions.

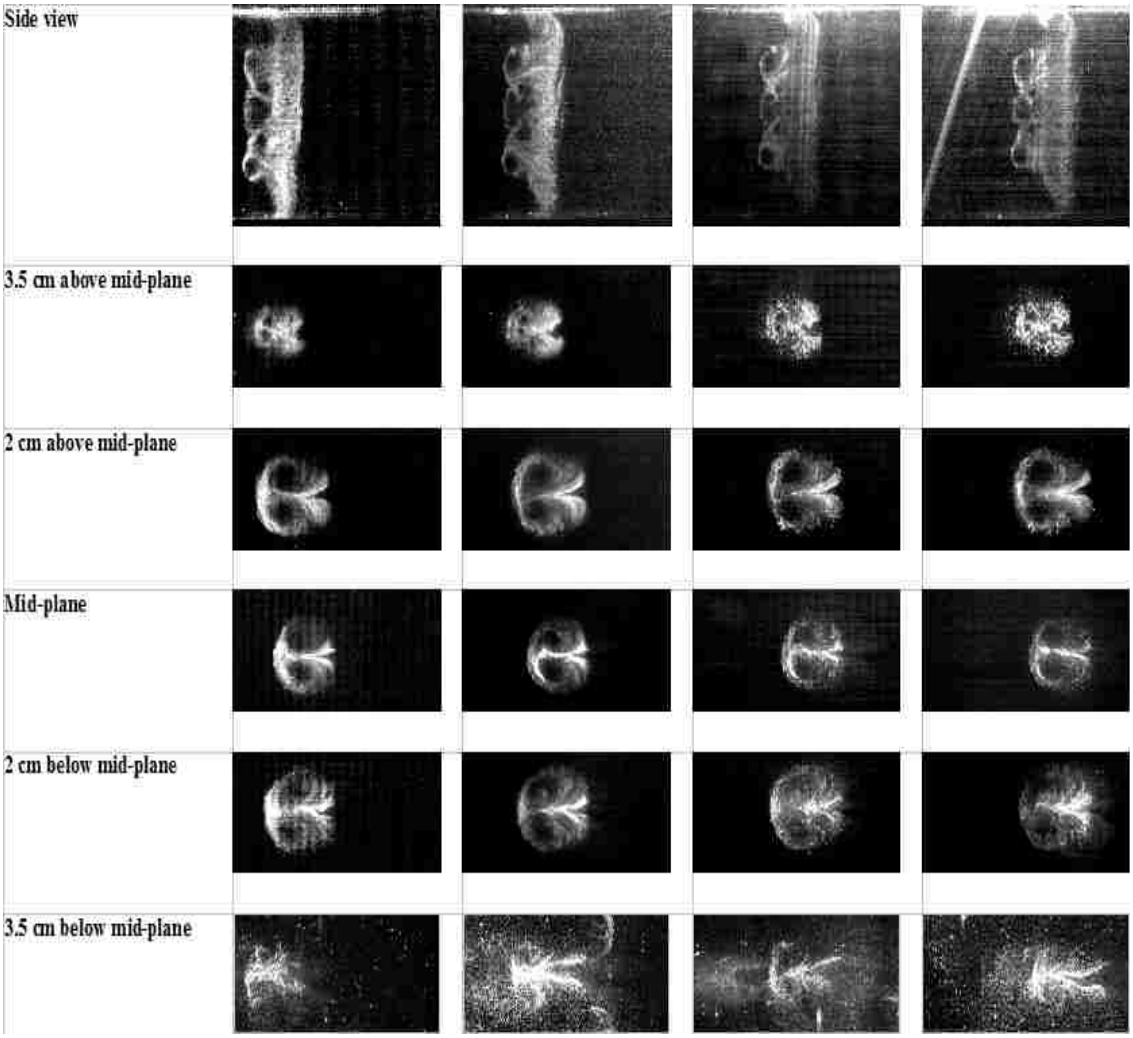

FIG. 27. Time evolution of a glycol SF_6-droplet column accelerated by a Mach 1.67 shock. Images are acquired at a downstream distance of 19 cm from the initial conditions. Shock direction is left to right. Time interval between images in each column is 50 μs, horizontal image extent is ~5 cm. The top row shows the view from the side, the five rows below it – images in stacked horizontal planes.

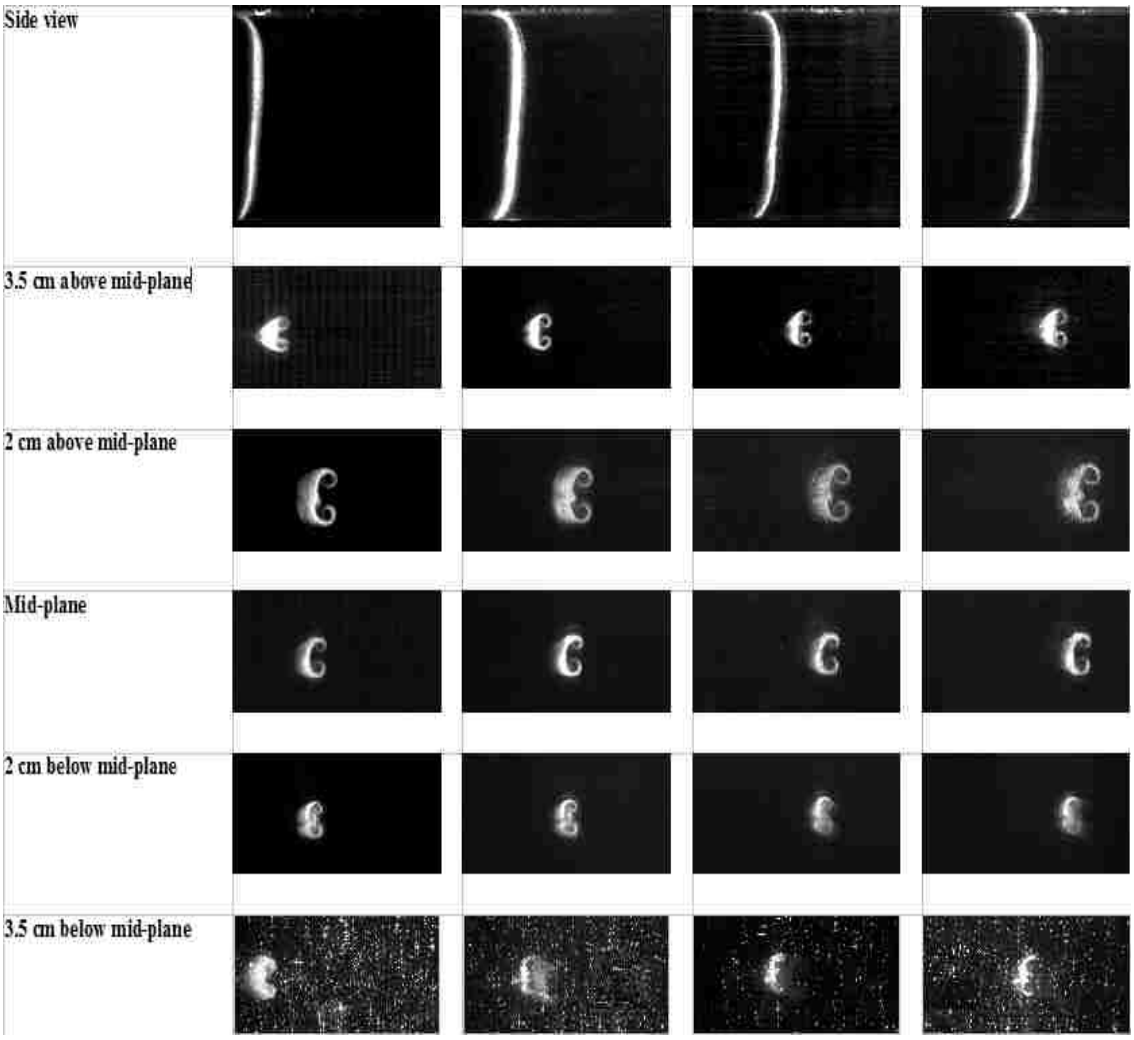

FIG. 28. Time evolution of a glycol air-droplet column accelerated by a Mach 1.67 shock. Images are acquired at a downstream distance of 19 cm from the initial conditions. Shock direction is left to right. Time interval between images in each column is 50 μs, horizontal image extent is ~5 cm. The top row shows the view from the side, the five rows below it – images in stacked horizontal planes.

Chapter 3. Results of Experiments

As the shock traverses over the hole, it is no longer perfectly planar in that region. It has been found [20] that the forced Korteweg-de Vries (fKdV) equation is an appropriate model to approximate the nonlinearity of supercritical flow past a hole. Numerical and asymptotic analytical solutions of the fKdV equation have demonstrated that for flow over a localized obstacle, in the transcritical regime the solution typically consists of an upstream and downstream nonlinear wavetrain. These nonlinear wavetrains have the structure of unsteady undular bore, which are commonly found in meteorology studies. An undular bore is a traverse wave that is perpendicular to energy transferred due to two air masses of differing temperatures colliding. When the shock traverses through the medium, there is a rise in temperature. This creates an undular bore near the injection site causing more non-linearity in the flow morphology. As you can see from the plane closest to the boundary in both Fig. 27 and Fig. 28 (3.5 mm from mid-plane), the amplitude of the perturbation width is smaller than for the case of mid-plane illumination. There is also an increase in particle concentration due to viscous effects in the flow.

The study of multiple planes is an area of RMI (or PLI) that requires more research and experimentation to fully understand the physics behind what is truly happening. Image ensembles can be used to determine a quantitative measure of the turbulent mixture regions in the flow. These ensembles will provide an understanding into transition to turbulence in a 3D sense. This is being considered currently as a possible research route at the University of New Mexico.

3.4 Particle Size Distribution

Numerical data has been collected suggesting strong importance of particle size distribution in the 2-phase medium. As you can see from Fig. 29 [19], the particle size determines the evolution of the flow and determines whether or not an instability will be produced after shock passage. This study suggests that there may be a critical particle size associated with PLI.

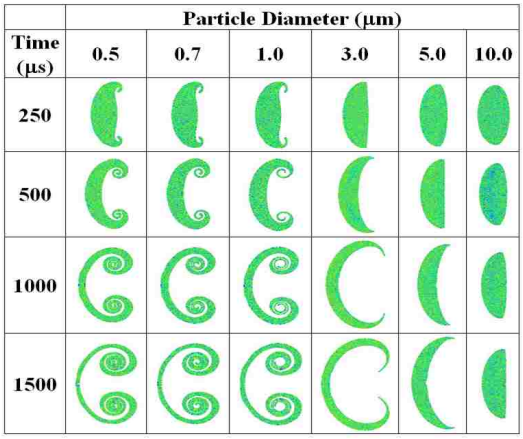

FIG. 29. Numerical mosaic of the flow morphology as a function of particle size - [19].

If the particles are sub-micron sized and dwell in the lower nanoscale range (< 20 nm, not shown), the volume fraction of particles in the injected column would be too large and therefore the vorticity deposition on the interface is baroclinic (or RMI). If the particles are too large (> 5 μm), they tend to act as one large particle in the flow and therefore drop off before any vortices are deposited on the interface. So, the critical values have been determined to be within 20 nm and 5 μm. This is clearly visible in the numerical data comparing different particle sizes.

Possessing the capability of directly measuring particle size both before and after shock acceleration is highly desirable. This would allow us to validate the numerical code as well as measure the particle concentration, which is a direct factor of PLI. This means that it may be possible to measure the particle lag distribution as a function of the measured particle size. This will clarify the features of strongly compressible initial interaction of the droplets with shock-accelerated gas. In theory, since the larger particles (> 4 μm) tend to trail in the flow due to a slower momentum exchange, the flow structure will consist of particle size varying from largest to smallest.

It is also advantageous to have the ability to vary the average size of the particles. Various particle sizes could be achieved by using customized aerosol attachments that would inject a continuous medium through the injection site. The speed of the aerosol jet would be relatively zero compared to the speed of the shock.

3.5 Geometry of the Initial Conditions

If the geometry of the injected material is initially (pre-shock) asymmetric, the morphology of the instability tends to be distorted and shows poor evolution of RMI and PLI. Figure 30 illustrates this phenomenon and shows the random scattering of particles that occurs. Vortices can still be seen in the flow, but there are other developments downstream from this.

Chapter 3. Results of Experiments

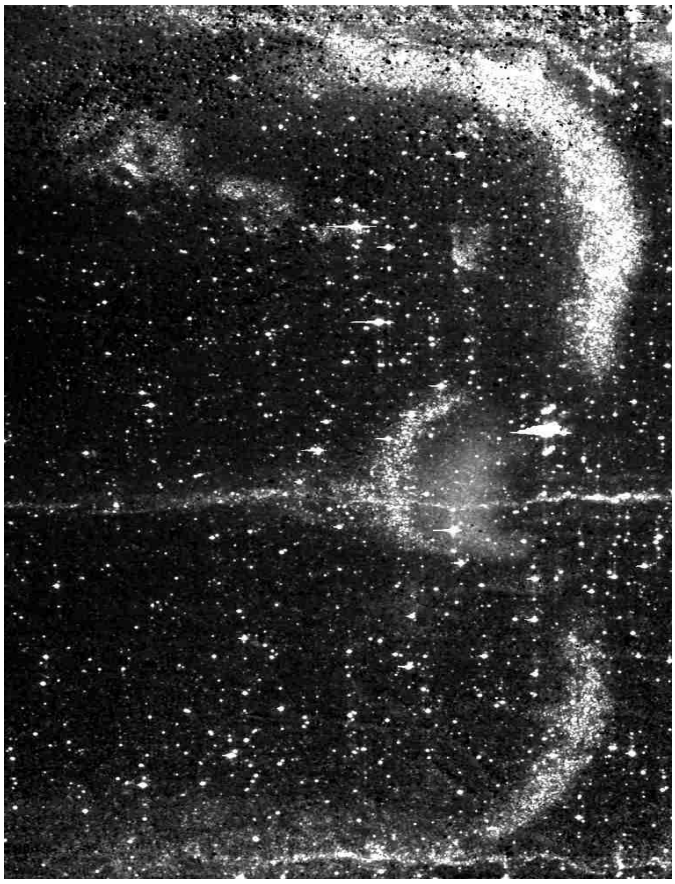

FIG 30. Flow morphology due to distorted initial conditions. Shock front was at M = 1.67 and is traveling from left to right.

A largely perturbed interface produces non-linear secondary instabilities whose evolution is difficult to quantify [21]. Complicated theoretical solutions have been developed that facilitate in the understanding of these secondary instabilities, however due to the fact that they produce singularities in the flow, the solutions are difficult to solve. The non-linear regime of RMI and PLI is not understood very well.

Multiple steps are taken to ensure that the initial conditions are perfectly cylindrical prior to each experiment. Before each experiment, the settling tank is wiped

clean of any glycol residue left behind from previous experiments and the injection nozzle is cleaned as well. A bucket of ice is located within the settling tank directly below the fog machine injection port. The ice keeps the temperature of the air-fog (or SF_6-fog) mixture lower than the surrounding air, as to negate any buoyancy effects. A light suction is sometimes applied to the bottom of the test section over the injection port if the IC's are not properly stabilized. If the IC's ever become unstable, each of these issues is assessed.

Chapter 4

Conclusion

4.1 Summary

In conclusion, Richtmyer-Meshkov instability (RMI) is the mixing of two fluids that arises due to shock-accelerating a density interface, which in turn develops a pair of counter-rotating vortices upon transitioning to turbulence. There are many different ways to model RMI in experiment, with a shock tube remaining the most commonly used system to show compressible RMI. Our experiments included the modeling of traditional compressible RMI, which then led to a new instability with RMI-like features. This is also known as particle lag instability (PLI) and shares similar characteristics to RMI, but with a different mechanism. We used a horizontal shock tube to show how the interaction of a planar shock wave affects particles suspended in air. This was all captured using state-of-the-art equipment including an Imacon CCD camera, an Apogee CCD camera, two double-pulsed green light lasers, and other advanced diagnostics.

After many experimental runs, we were able to distinguish some differences between “traditional” RMI and particle lag instability. One difference that can be easily seen by direct comparison of the images is the noticeable perturbation width difference. RMI has distinctively larger instability growth than PLI in the same downstream locations. This can be accredited to the effective Atwood number of PLI being measurably lower than the Atwood number of RMI. A width comparison study was

conducted that plotted the perturbation growth curves using dimensionless coordinates.

Multiple plane ensembles were constructed to create a 3-dimensional view of the instability. This gave insight to the effects of the shock tube walls, particularly near the injection site. As the shock passes the injection site, it creates non-linear wavetrains due to a rise in temperature. These wavetrains resemble undular bore, which are commonly found in meteorology studies. This creates more non-linearity in the flow near the boundary and affects the perturbation width amplitude.

It was also discovered that there might be a critical particle size for PLI. Numerical studies have authenticated this feature and show the morphology of the perturbation using different size particles. If the particles are too small (< 20 nm), shock-acceleration results in traditional RMI. If the particles are too large, they lag in the flow as a lump concentration of particles and drop out before an instability develops on the interface.

Non-linear geometries also have an effect on the dynamics of the instability. If they are initially distorted (non-cylindrical), they tend to cause secondary instabilities in the flow, which results in asymmetric vortices. Several precautions are taken to ensure perfectly stable IC's.

4.2 Future Work

Although this has yet to be studied in experiment, there is a desire to validate the numerical data gathered on particle size distribution. Having direct control over the

particle size and varying their sizes per experiment would be advantageous. Using customized aerosol attachments and directly spraying the droplets into the injection site could accomplish this. It would assess whether the instability strength decreases as particle size increases.

The growth perturbation curves were previously collapsed using the non-dimensionalized coordinate τ and w/w_0. However, recent numerical work [19] has suggested a non-dimensionalization involving the square root of the Mach number, which will provide a better collapse of the curves. Further data is desired to validate the new scaling and understand the physics behind it.

We have a good understanding of what is happening in RMI and PLI in the linear and non-linear regimes, but there is very little perceptive into the physics of the turbulent region. Studying the effects of re-shock would give insight to this unfamiliar area. After a sufficient amount of time, particles of every size attain equilibrium with the surrounding flow in terms of velocity. It is thought that the presence of particles and their distribution might delay a transition to turbulence due to the particles' ability to absorb energy. Understanding the context of this transition could be of fundamental importance in controlling their mixing characteristics. It would also be advantageous to create 3D ensembles generated from multiple planes to give an understanding of the 3-dimensional sense of transition to turbulence.

As we had hoped, our studies of complex shock-driven multiphase physics has led to advancement in RMI studies as well as an instability driven by a new underlying

mechanism. Our findings will lead to improved quality and a better understanding of RMI and PLI. Furthermore, a new proposal has been submitted and is currently in review and pending approval for grants from the NSF agency.

References

1. R.D. Richtmyer, Commun. Pure Appl. Math. 13, 297 (1960).
2. E.E. Meshkov, Sov. Fluid Dyn. 4, 101 (1969).
3. P. Vorobieff and S. Kumar, Recent Res. Devel. Fluid Dyn. 5, 33 (2004).
4. P. Vorobieff et al., PRL. 106, 184503 (2011).
5. R.L. Holmes et al., J. Fluid Mech. 389, 55 (1999).
6. J.W. (Lord Rayleigh) Strutt, Proc. London Math. Soc. 14, 170 (1883).
7. G.I. Taylor, Proc. R. Soc. London Ser. A – Math. 201 (no. 1065), 192 (1950).
8. L.D. Landau and E.M. Lifshitz. Fluid Mech. Butterworth-Heinemann. 2nd ed., Vol. 6 (1987).
9. B.J. Balakumar et al., Phys. Fluids 20, 124103 (2008).
10. I.G. Currie, Fund. Mech. of Fluids, 3rd ed., Chap. 8. Taylor & Francis Group, Boca Raton, FL (2003).
11. C.E. Cockrell, Jr., et al., AIAA, 2002-5188 (2002).
12. J.W. Jacobs and J.M. Sheeley, Fluid Mech. 8, 405 (1996).
13. J.W. Jacobs, M.A. Jones, and C.E. Niederhaus. Inter. Work. on Compress. Turb. Mix. 1, 195 (1996).

References

14. S. Kumar et al., Phys. Fluids 17, 082107 (2005).

15. G.C. Orlicz et al., Phys. Fluids 21, 064102 (2009).

16. P.M. Rightley, P. Vorobieff, and R.F. Benjamin, Phys. Fluids 9, 1770 (1997).

17. J.W. Jacobs et al., J. Fluid Mech. 295, 23 (1995).

18. M.K. Parmar, A. Haselbacher, and S. Balachandar, AIAA Paper, 2009-1124 (2009).

19. M. Anderson, Ph.D. Dissertation, The University of New Mexico (2011).

20. R.H.J. Grimshaw, D.H. Zhang, K.W. Chow, Studies in Appl. Math. 122, 235 (2009).

21. S.I. Abarzhi, Phys. Rev. E 66, 036301 (2002).